Doping site induced alteration of incommensurate antiferromagnetic ordering in Fe-doped MnNiGe alloys

R. Roy,[1] S. K. Adhikari,[1] J. Sannigrahi,[2,3] K. Mandal,[1] S. C. Das,[1] P. Dutta,[1,4] S. Pramanick,[1] D. Khalyavin,[3] D. T. Adroja,[3,5] and S. Chatterjee[1,*]

[1]*UGC-DAE Consortium for Scientific Research, Kolkata Centre, Sector III, LB-8, Salt Lake, Kolkata 700106, India*

[2]*School of Physical Sciences, Indian Institute of Technology Goa, Ponda 403401, Goa, India*

[3]*ISIS Facility, Rutherford Appleton Laboratory, Chilton, Didcot OX11 0QX, United Kingdom*

[4]*New Chemistry Unit and School of Advanced Materials, Jawaharlal Nehru Centre for Advanced Scientific Research, Jakkur, Bangalore 560064, India*

[5]*Highly Correlated Matter Research Group, Physics Department, University of Johannesburg, PO Box 524, Auckland Park 2006, South Africa*

(Received 7 September 2021; accepted 22 November 2021; published 6 December 2021)

The magnetic structure of Fe-doped MnNiGe alloys of nominal compositions $MnNi_{0.75}Fe_{0.25}Ge$ and $Mn_{0.85}Fe_{0.15}NiGe$ has been explored through detailed neutron powder diffraction (NPD) study in ambient and high-pressure (6 kbar) conditions. Both these alloys crystallize with Ni_2In-type hexagonal structure (with $P6_3/mmc$ space group) at room temperature and undergo a martensitic transition to low-temperature TiNiSi-type orthorhombic structure (with space group *Pnma*). Both the alloys show incommensurate antiferromagnetic ordering at the low-temperature martensitic phase. However, the modulation of the magnetic structures depends strongly on the doping site of Fe. The incommensurate propagation vector **k** for $MnNi_{0.75}Fe_{0.25}Ge$ and $Mn_{0.85}Fe_{0.15}NiGe$ alloys are found to be (0.1790(1),0,0) and (0.1543(3),0,0), respectively at 1.5 K, and these remain almost unchanged with increasing sample temperature under ambient conditions. The application of the external pressure results in a significant effect on both martensitic transition temperature and low-temperature magnetic structure. The propagation vectors **k** for both the alloys show a monotonic decrease with increasing sample temperature in the presence of external pressure. Interestingly, no sign of the magnetically ordered hexagonal austenite phase was observed in any alloys down to the lowest measurement temperature.

DOI: 10.1103/PhysRevB.104.214405

I. INTRODUCTION

The magnetic equiatomic alloys (MEAs) with general formula $MM'X$ (where M and M' are transition metals, and X is a nonmagnetic sp element) and their derivatives, identified as the new class of shape memory alloy, have gained significant interest among researchers not only for the shape memory property, but also for their diverse magneto-functionality, which includes a sizable magnetocaloric effect, magnetoresistance, the exchange bias effect, and so on [1–19]. MnNiGe is one of the prime members of the MEA family that experiences a martensitic-type structural transition around 470 K from high-temperature (T) hexagonal austenite phase (Ni_2In-type structure with space group $P6_3/mmc$) to low-T orthorhombic martensite phase (TiNiSi-type structure with space group *Pnma*) and ordered antiferromagnetically below 346 K [1,3,4,8,20–24]. A neutron powder diffraction (NPD) study indicated the spiral modulation of the antiferromagnetically ordered martensite phase [20]. In addition, a rotation of the axis of the spiral antiferromagnetic structure was also observed from the a-axis to the bc plane below 185 K [20]. In the magnetically ordered state at 80 K, the Mn-site moment size is around 2.75 μ_B [20]. To achieve enhanced functionality, researchers adopted various doping strategies to tune these structural and magnetic transition temperatures, including (i) doping of foreign elements at different sites of the alloy and (ii) self doping [1,3–5,7,8,13–19,25–27]. As is evident from the recent studies, Mn/Ni site doped alloys retain the antiferromagnetic (AFM) ordering of the low-T martensite phase. NPD studies confirm the helically modulated incommensurate AFM ordering in Ti/Cr doped MnNiGe alloys [22–24]. Ge-site doping, on the other hand, behaves differently. A recent NPD study indicated the transition from a commensurate AFM austenite to a helically modulated incommensurate AFM martensite phase in Ge-site doped alloys [28].

Among others, Fe doping in the Mn or Ni site is particularly important due to the broad tunability of martensitic phase transition (MPT) and rich magneto-functional behavior [4,8,13–15]. The absence of MPT in isostructural MnFeGe and FeNiGe results in a stable austenite phase down to the lowest-T of measurement and plays a crucial role behind the decrease in MPT [29]. Liu *et al.* recently performed a detailed study on the effect of Fe doping on the Mn and Ni-sites of the MnNiGe alloy and confirmed the increase in ferromagnetic (FM) interaction with increasing Fe-concentration in an otherwise AFM alloy [8]. The observed conclusions regarding the magnetic ground state of the Fe-doped alloys are entirely

*souvik@alpha.iuc.res.in; souvik@csr.res.in

based on the macroscopic measurements. Up until now, no microscopic measurements have yet been performed to probe the true magnetic character of these materials. Our recent works revealed several exciting properties of Fe-doped MnNiGe alloys in ambient and high-pressure conditions [4,13–15]. As the magnetic structure plays a crucial role in observing different magneto-functional behaviors, it is pertinent to investigate the exact magnetic structure of these Fe-doped MnNiGe alloys.

In the present work, our main aim is to focus on the magnetic structure of two Fe-doped MnNiGe alloys of nominal compositions $MnNi_{0.75}Fe_{0.25}Ge$ and $Mn_{0.85}Fe_{0.15}NiGe$ through detailed NPD studies in ambient as well as in high-pressure conditions. The application of external pressure (P) is the cleanest form of perturbation, and the NPD study in high-pressure situations will give us a comprehensive idea about the effect of increasing Fe concentration on the magnetic structure of these alloys as Fe-doping results in a positive chemical pressure in the system (evident from the decrease in lattice parameter with increasing Fe concentration both in Mn and Ni-sites) [8]. Our NPD results confirm a helically modulated incommensurate antiferromagnetic structure of the low-T martensitic phase for the Ni-site Fe-doped alloy. On the other hand, the magnetic ground state of the Mn-site doped alloy is of cycloidal type, and with increasing sample temperature, it transforms to a helically modulated structure. The incommensurate propagation vector experiences a significant change in the presence of external P. Such a change in incommensurate propagation vector directly affects the AFM ordering in the presently studied alloys. However, we have not noticed any FM arrangement in any of the presently studied Fe-doped MEAs, at least in the absence of an external magnetic field.

II. EXPERIMENTAL DETAILS

The presently studied Fe-doped MnNiGe alloys of nominal compositions $MnNi_{0.75}Fe_{0.25}Ge$ and $Mn_{0.85}Fe_{0.15}NiGe$ were prepared in the polycrystalline form by melting the required amount of constituent elements (purity $> 99.9\%$) in an argon atmosphere using a Centorr make tri-arc furnace. The melting process for both these alloys was repeated four times to achieve the desired homogeneity in the alloys. Finally, the ingots were kept in evacuated quartz ampoules and annealed at 800° C for 100 h followed by quenching in ice water. For the rest of this article, we shall use MNFG and MFNG abbreviations for $MnNi_{0.75}Fe_{0.25}Ge$ and $Mn_{0.85}Fe_{0.15}NiGe$ alloys, respectively.

The NPD studies were performed at the ISIS Facility (Rutherford Appleton Laboratory) in the UK, using the cold neutron (time of flight) diffractometer WISH [30]. The powder samples were mounted in a 6-mm vanadium cell for the ambient pressure experiment and cooled down to 1.5 K using a standard He cryostat. We used a TAV6 gas cell (Ti-6Al-4V-alloy) with an internal diameter of 7 mm, attached to the automated intensifier system for high-pressure NPD experiments, where high-pressure He gas was used as the pressure media. In this method, one can apply up to 10 kbar uniform pressure (P) on the sample. The pressure cell was inserted into the He cryostat and cooled down to 10 K. Data were collected at different constant temperatures (T) in the warming cycle. We used ∼5 g powder of MNFG and MFNG alloys for both ambient and high-pressure NPD measurements. Long scans of about 30 minutes were used for magnetic structure determination for both the alloys in ambient conditions. We also recorded several quick scans of 5 min duration each for order parameter determination. The constituent elements of the presently studied alloys are very good neutron scatterers, which is clear from the reported neutron scattering cross-section data [Mn → 2.15(3) barn, Ni → 18.50(3) barn, Ge → 8.60(6) barn, and Fe → 11.62(10) barn] [31]. The FULLPROF software package was used for refining the NPD data [32]. On the other hand, for creating and visualizing the magnetic structure model, we used the BASIREPS and VESTA software packages.

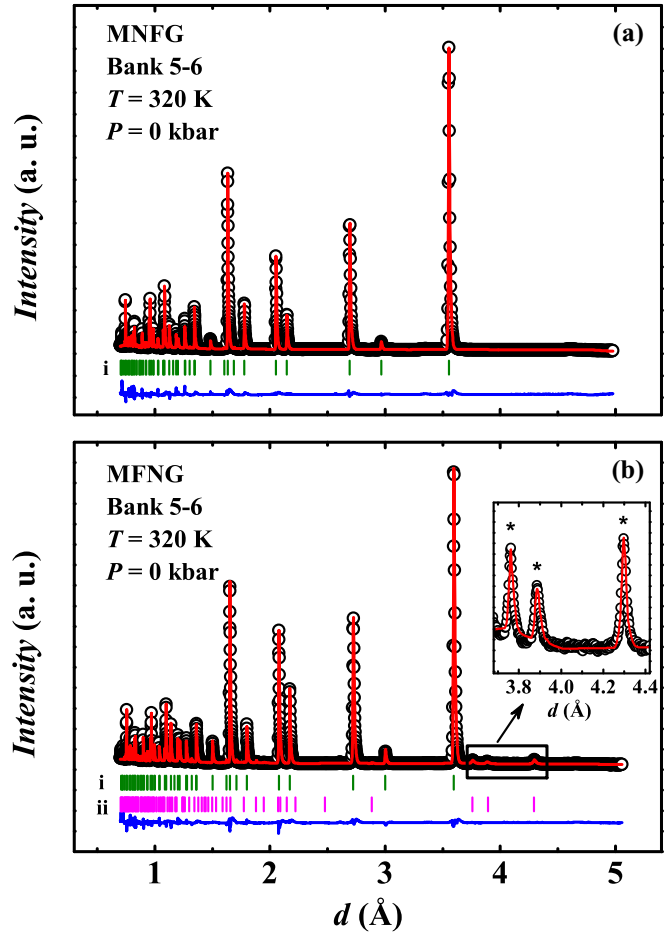

FIG. 1. Main panels of (a) and (b) show NPD data from 5–6 detector bank of WISH, recorded at 320 K, for $MnNi_{0.75}Fe_{0.25}Ge$ (MNFG) and $Mn_{0.85}Fe_{0.15}NiGe$ (MFNG) alloys, respectively. Here the observed, calculated, and difference patterns are represented by black circles, red lines, and blue lines (lowermost lines in the main panels), respectively. The olive (labeled i) and magenta (marked ii) vertical bars represent the peak positions for the Ni_2In-type (for MNFG and MFNG) and $MgZn_2$-type (for $MnNi_{1.3}Ge_{0.7}$) hexagonal nuclear phases, respectively. Inset of (b) shows the enlarged view of the nuclear reflections originating from the $MnNi_{1.3}Ge_{0.7}$ composition.

TABLE I. The structural parameters obtained from the refinement analysis at 1.5 K and 320 K for $MnNi_{0.75}Fe_{0.25}Ge$ (MNFG) and $Mn_{0.85}Fe_{0.15}NiGe$ (MFNG) alloys are listed. MFNG alloy is associated with an additional $MnNi_{1.3}Ge_{0.7}$ phase with following weight percentages:−1.01(±0.07)% at 1.5 K and 1.12(±0.09)% at 320 K.

$MnNi_{0.75}Fe_{0.25}Ge$ at $T = 1.5$ K						$Mn_{0.85}Fe_{0.15}NiGe$ at $T = 1.5$ K					
$R_p = 6.57\%$ & $R_{wp} = 7.41\%$						$R_p = 6.83\%$ & $R_{wp} = 8.31\%$					
TiNiSi-type orthorhombic structure with space group *Pnma*											
$a = 5.994(1)$ Å	$b = 3.749(7)$ Å	$cw = 7.123(6)$ Å				$a = 5.976(1)$ Å	$b = 3.713(8)$ Å	$c = 7.065(4)$ Å			
Bragg *R*-factor: 6.11%	Phase fraction = 99.52(±1.27)%					Bragg *R*-factor: 5.68%	Phase fraction = 97.95(±0.80)%				
Type	Site	*x*	*y*	*z*	B_{iso}	Type	Site	*x*	*y*	*z*	B_{iso}
Mn	4*c*	0.030(4)	0.250	0.180(5)	1.73(6)	Mn	4*c*	0.034(3)	0.250	0.185(4)	1.11(5)
Ni	4*c*	0.149(8)	0.250	0.557(2)	0.88(1)	Fe	4*c*	0.034(3)	0.250	0.185(4)	1.11(5)
Fe	4*c*	0.149(8)	0.250	0.557(2)	0.88(1)	Ni	4*c*	0.146(8)	0.250	0.556(5)	1.51(2)
Ge	4*c*	0.758(7)	0.250	0.625(3)	0.95(3)	Ge	4*c*	0.754(4)	0.250	0.628(9)	0.89(7)
Ni_2In type hexagonal structure with space group $P6_3/mmc$											
$a = 4.088(6)$ Å	$c = 5.319(8)$ Å	$\gamma = 120^\circ$				$a = 4.060(1)$ Å	$c = 5.347(6)$ Å	$\gamma = 120^\circ$			
Bragg *R*-factor: 8.15%	Phase fraction = 0.48(±0.06)%					Bragg *R*-factor: 5.4%	Phase fraction = 1.04(±0.11)%				
Type	Site	*x*	*y*	*z*	B_{iso}	Type	Site	*x*	*y*	*z*	B_{iso}
Mn	2*a*	0.000	0.000	0.000	1.37(8)	Mn	2*a*	0.000	0.000	0.000	1.37(7)
Ni	2*d*	0.333	0.666	0.750	1.04(9)	Fe	2*a*	0.000	0.000	0.000	1.37(7)
Fe	2*d*	0.333	0.666	0.750	1.04(9)	Ni	2*d*	0.333	0.666	0.750	2.48(8)
Ge	2*c*	0.333	0.666	0.250	0.68(9)	Ga	2*c*	0.333	0.666	0.250	2.21(8)
$MnNi_{0.75}Fe_{0.25}Ge$ at $T = 320$ K $R_p = 8.73\%$ & $R_{wp} = 11.0\%$						$Mn_{0.85}Fe_{0.15}NiGe$ at $T = 320$ K $R_p = 8.28\%$ & $R_{wp} = 11.7\%$					
Ni_2In type hexagonal structure with space group $P6_3/mmc$											
$a = 4.104(3)$ Å	$c = 5.385(7)$ Å	$\gamma = 120^\circ$				$a = 4.072(1)$ Å	$c = 5.339(7)$ Å	$\gamma = 120^\circ$			
Bragg *R*-factor: 6.19%	Phase fraction = 100.00%					Bragg *R*-factor: 12.5%	Phase fraction = 98.88(±1.15)%				
Type	Site	*x*	*y*	*z*	B_{iso}	Type	Site	*x*	*y*	*z*	B_{iso}
Mn	2*a*	0.000	0.000	0.000	1.31(8)	Mn	2*a*	0.000	0.000	0.000	1.49(6)
Ni	2*d*	0.333	0.666	0.750	0.84(5)	Fe	2*a*	0.000	0.000	0.000	1.49(6)
Fe	2*d*	0.333	0.666	0.750	0.84(5)	Ni	2*d*	0.333	0.666	0.750	0.55(7)
Ge	2*c*	0.333	0.666	0.250	0.54(9)	Ga	2*c*	0.333	0.666	0.250	0.12(3)

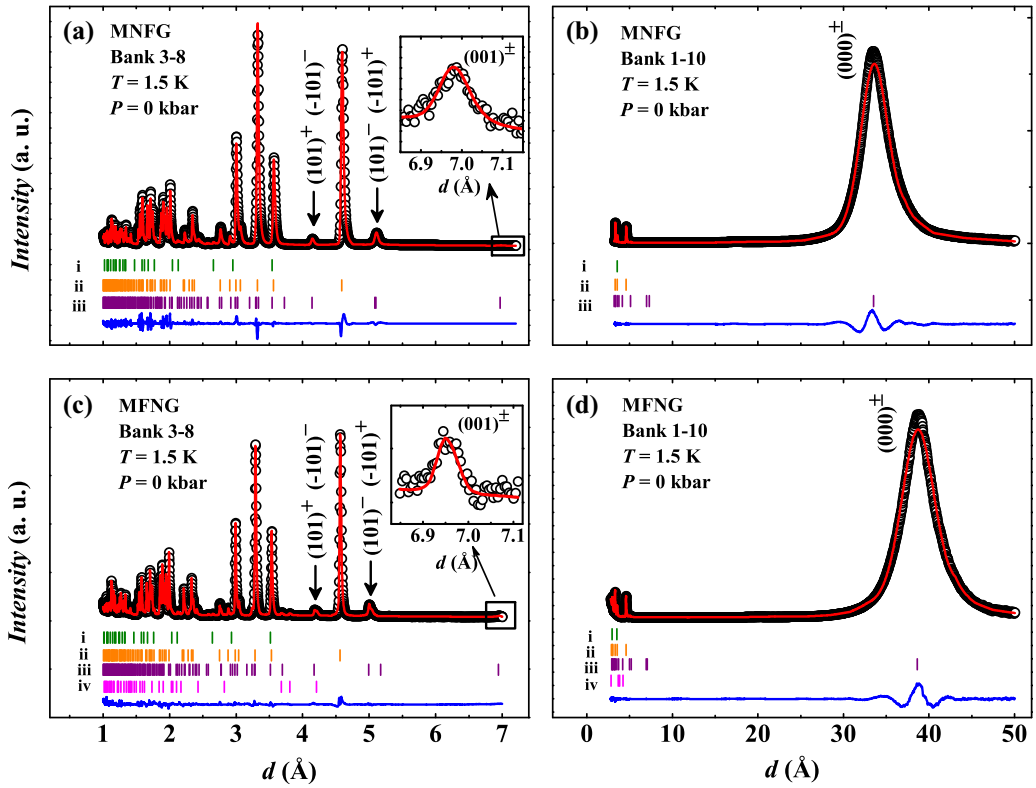

FIG. 2. NPD patterns for (a), (b) MNFG and (c), (d) MFNG alloys recorded at 1.5 K at ambient pressure (samples mounted in 6-mm vanadium cell) from 3–8 and 1–10 detector banks of WISH are plotted for two different lattice spacing (d) ranges. The enlarged view of the $(001)^{\pm}_{o}$ magnetic reflection is shown in the insets of (a) and (c). Here the black circles, red lines, and blue lines represent observed, calculated, and difference patterns, respectively. The vertical bars represent the peak positions for the Ni_2In-type hexagonal nuclear phase (olive, labeled i), TiNiSi-type orthorhombic nuclear phase (orange, labeled ii), orthorhombic magnetic phase (purple, marked iii), and $MgZn_2$-type hexagonal nuclear phase (magenta, marked iv).

III. EXPERIMENTAL RESULTS

A. Room-temperature neutron diffraction

We recorded NPD data at 320 K (around room temperature) for both MNFG and MFNG alloys in the ambient pressure and plotted in Figs. 1(a) and 1(b), respectively. Ni_2In-type hexagonal structure with space group $P6_3/mmc$ of the room-temperature austenite phase for both the alloys is clear from the Rietveld refinement analyses of the recorded data. A minute inspection of the MFNG NPD pattern indicates the presence of some additional reflections [see inset of Fig. 1(b)]. The presence of $MgZn_2$-type hexagonal $MnNi_{1.3}Ge_{0.7}$ alloy along with the MFNG is responsible for such reflections. About 1.12(±0.09) wt % of the $MnNi_{1.3}Ge_{0.7}$ alloy is found to be present in the MFNG alloy around room temperature. The coexistence of $MnNi_{1.3}Ge_{0.7}$ and MEAs are pretty standard and already reported in the literature [28,33]. However, MNFG is found to be free of such $MnNi_{1.3}Ge_{0.7}$ alloy (as we did not observe any traces of the reflections corresponding to $MgZn_2$-type hexagonal structure). The absence of any magnetic satellite reflection confirms the nonmagnetic character of MNFG, MFNG, and $MnNi_{1.3}Ge_{0.7}$ alloys at/around room temperature (320 K). The hexagonal lattice parameters obtained for all these alloys [MNFG: $a_h = 4.104(3)$Å, $c_h = 5.385(7)$Å, MFNG: $a_h = 4.072(1)$Å, $c_h = 5.339(7)$Å, and $MnNi_{1.3}Ge_{0.7}$: $a_h = 4.860(3)$Å, $c_h = 7.614(3)$Å] are found to match well with the similar MEAs reported previously [8,28,33]. Various refinement parameters at 320 K are compiled in Table I.

B. Magnetic structure identification

To shed light on the magnetic structure of the presently studied alloys, we recorded NPD data at 1.5 K in ambient conditions. The NPD data for two different lattice spacing (d) ranges along with the refinement patterns are plotted in Figs. 2(a) and 2(b) for MNFG and Figs. 2(c) and 2(d) for MFNG. The majority of the peaks observed in the NPD patterns belong to the low-T TiNiSi-type orthorhombic structure (space group *Pnma*). However, apart from the orthorhombic reflections, some additional reflections are also visible for both the alloys. Such additional peaks correspond to (i) nuclear reflections from high-T hexagonal and $MnNi_{1.3}Ge_{0.7}$ phases and (ii) magnetic satellite reflections. Our analyses confirm the presence of about 0.48 (±0.06) and 1.04 (±0.11) wt% of high-T Ni_2In-type hexagonal phase at 1.5 K for MNFG and MFNG alloys, respectively. The existence of high-T austenite phase is not uncommon for MEAs and is already reported for different alloys belonging to this family [15,16,28]. No significant change in the weight percent of $MnNi_{1.3}Ge_{0.7}$ phase, present with the MFNG alloy, has been observed. Notably, the position of the most intense magnetic

TABLE II. The incommensurate antiferromagnetic structures for $MnNi_{0.75}Fe_{0.25}Ge$ (MNFG) and $Mn_{0.85}Fe_{0.15}NiGe$ (MFNG) alloys were defined as $(R\mathbf{v} + iI\mathbf{w})e^{-2\pi i(\mathbf{k}.\mathbf{t}+\varphi)}$. Here, the real and imaginary parts of the Fourier coefficients are indicated by R and I, respectively, $\mathbf{t}$ is lattice translation, and φ is the magnetic phase. The plane of spin rotation is defined by the unit vectors $\mathbf{v}$ and $\mathbf{w}$. The Fourier coefficients for MNFG and MFNG alloys at 1.5 K for ambient pressure (propagation vector $\mathbf{k}$ = (0.1790(1),0,0) and (0.1543(3),0,0) for MNFG and MFNG alloys, respectively) and at T = 10 K for P = 6 kbar (propagation vector $\mathbf{k}$ = (0.1569(1),0,0) and (0.1404(8),0,0) for MNFG and MFNG alloys, respectively) are listed here.

Mn-site	Moment size, $R = I$ (μ_B)		Magnetic phase, φ	
	$MnNi_{0.75}Fe_{0.25}Ge$			
	$P = 0$, $T = 1.5$ K	$P = 6$ kbar, $T = 10$ K	$P = 0$, $T = 1.5$ K	$P = 6$ kbar, $T = 10$ K
Mn_{11}(0.0304,0.2500,0.1805)	3.09(3)	3.02(2)	0.000(0)	0.000(0)
Mn_{12}(0.5304,0.2500,0.3195)	3.09(3)	3.02(2)	0.089(5)	0.078(1)
Mn_{21}(0.4796,0.7500,0.6805)	3.09(3)	3.02(2)	0.099(1)	0.088(1)
Mn_{22}(0.9696, −0.2500, −0.1805)	3.09(3)	3.02(2)	0.188(1)	0.166(1)
	$Mn_{0.85}Fe_{0.15}NiGe$			
	$P = 0$, $T = 1.5$ K	$P = 6$ kbar, $T = 10$ K	$P = 0$, $T = 1.5$ K	$P = 6$ kbar, $T = 10$ K
Mn_{11}(0.0343,0.2500,0.1854)	2.63(6)	3.29(2)	0.000(0)	0.000(0)
Mn_{12}(0.5343,0.2500,0.3145)	2.63(6)	3.29(2)	0.077(7)	0.070(2)
Mn_{21}(0.4656,0.7500,0.6854)	2.63(6)	3.29(2)	0.087(7)	0.080(2)
Mn_{22}(0.9656, −0.2500, −0.1854)	2.63(6)	3.29(2)	0.164(4)	0.150(4)

reflection is found to be at very high d ($d \sim 33.4$ Å for MNFG and $d \sim 38.7$ Å for MFNG), which is due to a more significant value of the magnetic form factor of Mn at larger d or smaller Q ($= \frac{2\pi}{d} \sim 0.188$ Å^{-1} for MNFG and ~0.162 Å^{-1} for MFNG). The observation of such high values of d for the most intense satellite peak is consistent with some other alloys of the MEA family also [23,24,28]. We successfully indexed the magnetic reflections for both MNFG and MFNG alloys by the incommensurate propagation vector $\mathbf{k} = (k_a,0,0)$ with k_a = 0.1790(1) and 0.1543(3) at 1.5 K, respectively, having orthorhombic structures. The refinement parameters at 1.5 K for both the alloys in ambient pressure are depicted in Table I. Notably, unlike Ge-site doped MnNiGe alloys, we did not observe any contribution from the magnetically ordered hexagonal austenite phase in the NPD pattern at 1.5 K [28].

The refinement of the magnetic structure was assisted by symmetry arguments based on the space group representation theory [34–36]. We tested all possible models for the magnetic structure and confirmed that all Mn atoms are fully ordered, having equal moments at all Mn sites. The wave vector group splits the 4c Mn position into two orbits, 1 and 2, and they are denoted as Mn_{11}, Mn_{12}, and Mn_{21}, Mn_{22} (see Table II). The x-coordinate of the two Mn sites in each orbit differs by 0.5, implying the phase difference $\frac{k_a}{2}$. The magnetic phase between the orbits is not fixed by the propagation vector and was determined from the refinement. It was possible since the intensity of the $(001)^{\pm}$ satellite was found to be very sensitive to the dephasing between the orbits. The models which provided the best fitting quality (the reliability factor R_{mag} = 3.99% and 2.41% for MNFG and MFNG alloys, respectively) were (i) helical structure with the spins rotating within the bc-plane for MNFG alloy and (ii) cycloidal-type structure with the rotation of the spins within the ab-plane for the MFNG alloy. The magnetic structure for both the alloys are depicted in Fig. 3. The parameters of the magnetic structure refined at T = 1.5 K are summarized in Table II. The helical modulation results in a rotation of the Mn moment along the a direction in the bc-plane [see Fig. 3(b)]. The angle (α) between two adjacent Mn moments is found to be ≈32.15° for the MNFG alloy. On the other hand, for the cycloidal modulation in the MFNG alloy, rotation of the Mn moments are constrained in the ab-plane [see Fig. 3(e)] with $\alpha \approx 28.26°$. Notably, no ordered moment

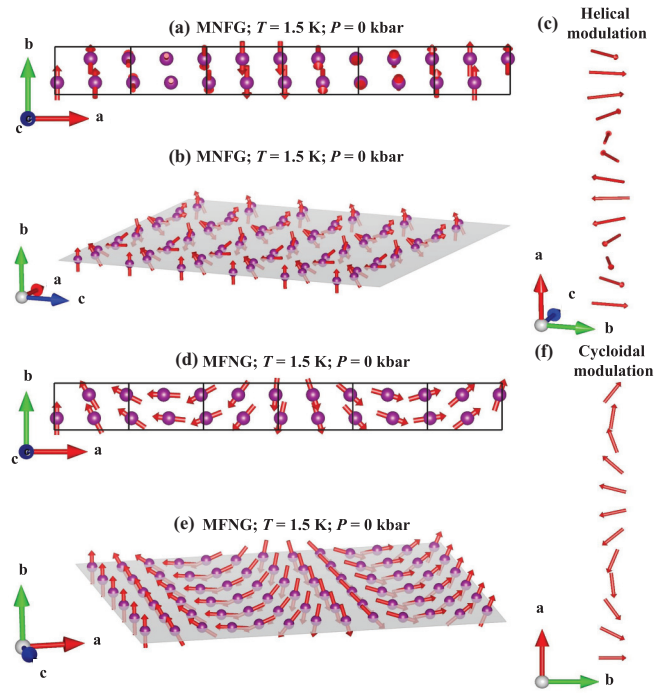

FIG. 3. (a), (b) and (d), (e) show the illustration of the helical and cycloidal magnetic structure at 1.5 K in ambient conditions for MNFG and MFNG alloys, respectively. The schematic representation of helical and cycloidal modulation of magnetic moments are depicted in (c) and (f), respectively.

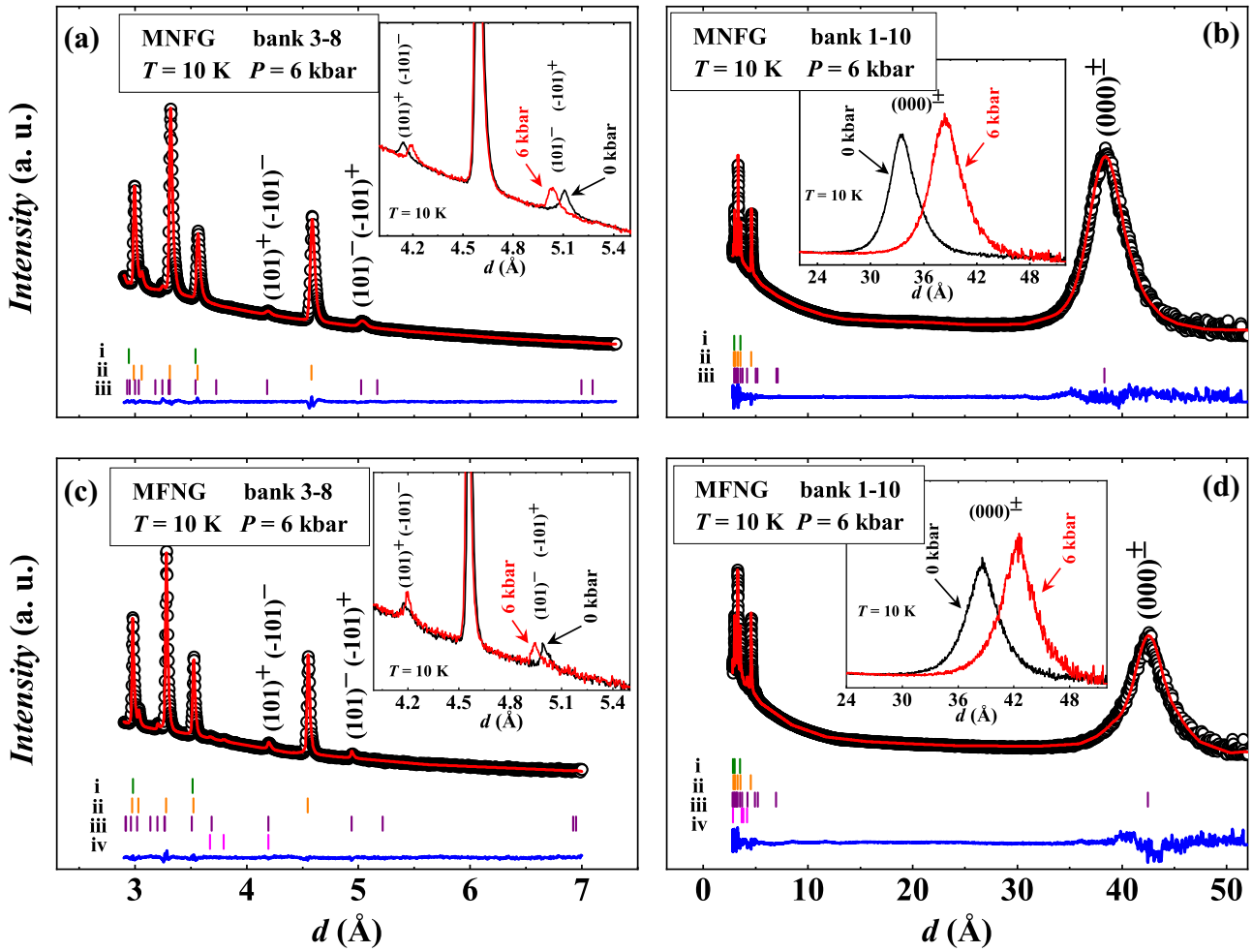

FIG. 4. NPD patterns recorded (black circles) from 3–8 and 1–10 detector banks of WISH in the presence of 6 kbar of external pressure (P) at 10 K for (a), (b) MNFG and (c), (d) MFNG along with the calculated (red lines) and difference patterns (blue lines) are plotted for two different d ranges. Insets depict the enlarged view of the magnetic reflections recorded in ambient and high P conditions at 10 K. The vertical bars, olive (labeled i), orange (labeled ii), purple (labeled iii), and magenta (labeled iv) represent the position of reflections from Ni_2In-type hexagonal nuclear phase, TiNiSi-type orthorhombic nuclear phase, orthorhombic magnetic phase, and $MnZn_2$-type hexagonal nuclear phase, respectively.

on the Fe atoms was detected from the NPD analysis in the MNFG alloy. However, Fe-doping in the Mn-site (magnetic site) drastically affects the magnetic structure of the alloy, and the modulation becomes cycloidal instead of helical, generally observed for the MEAs [21–24,28].

C. Effect of pressure on the magnetic structure

Let us now concentrate on the effect of external P on the magnetic structure of the presently studied Fe-doped MEAs. We recorded NPD data at 10 K for both MNFG and MFNG alloys in the presence of 6 kbar of external P. The diffraction patterns for two different d ranges are plotted in Fig. 4. For comparison, we also added the 10 K ambient pressure data in the insets of all the panels of Fig. 4. Minute inspection of the high-P NPD data recorded at 10 K confirms the absence of any new set of magnetic Bragg reflections compared with ambient P in any of the alloy (see main panels of Fig. 4). As a result, the high-P nuclear structure bears a strong resemblance to that of ambient pressure. Interestingly, the positions of magnetic reflections change significantly as compared to ambient pressure patterns: (i) $(101)^+$, $(-101)^-$, and $(000)^\pm$ reflections shifted towards higher d values and (ii) $(101)^-$, and $(-101)^+$ reflections shifted towards lower d values. Such behavior implies that the new propagation vector is still $\mathbf{k} = (k_a, 0, 0)$ but with a different k_a value (see insets of Fig. 4 for the closure look of magnetic reflections for ambient and high-pressure data). Besides, a shift in nuclear reflections also confirms the decrease in orthorhombic lattice parameters in the presence of an external P. At 10 K we can index all magnetic reflections in the high P NPD patterns with $k_a = 0.1569(1)$ and $0.1404(8)$ for MNFG and MFNG alloys, respectively. We, therefore, propose a similar noncollinear magnetic structure with helical and cycloidal modulation of Mn spins for MNFG and MFNG alloys, respectively, as that to the ambient pressure magnetic structures. We obtain an excellent agreement between observed and calculated intensities. The refined parameters of the magnetic structure at 10 K in the presence of 6 kbar of P for both the alloys are summarized in Table II. The magnetic structure obtained from our refinement

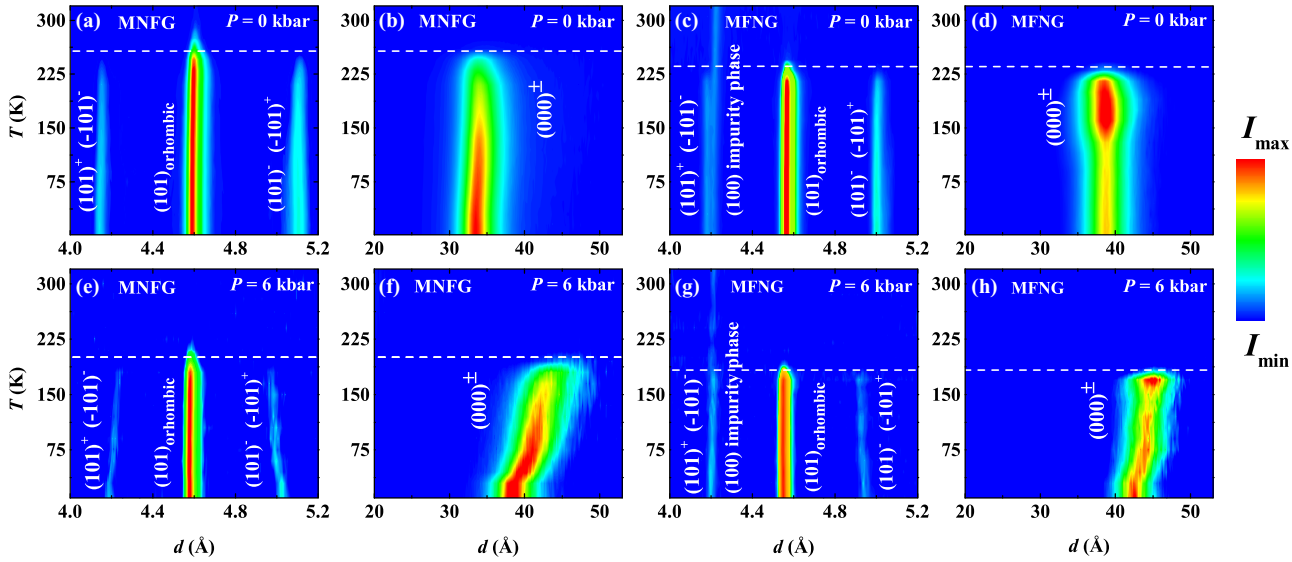

FIG. 5. Contour plots of the temperature (T) evolution of $(101)^+$, $(-101)^-$, $(101)^-$, $(-101)^+$, and $(000)^\pm$ magnetic satellite reflections at ambient pressure are plotted in (a), (b) for MNFG and (c), (d) for MFNG alloys. Contour plots in the presence of 6 kbar of external pressure for the T evolution of the same set of magnetic satellite reflections are depicted in (e), (f) for MNFG and (g), (h) for MFNG alloys. Normalized intensity is indicated by the right-side scale bar. White dotted horizontal lines indicate the martensitic phase transition temperature.

analyses indicate a decrease in α for both type of modulations in the high-pressure situation. For MNFG and MFNG alloys, α is found to be 28.15° and 26.57°, respectively, at 10 K under 6 kbar of external P.

D. Temperature evolution of magnetic structure in an ambient and high-pressure situation

We also probed the T evolution of the magnetic structure for the presently studied MNFG and MFNG alloys in ambient as well as in high-P conditions by recording NPD patterns at different constant T during warming. Contour plots of some restricted regions of such NPD patterns are presented in Figs. 5(a) and 5(b) and Figs. 5(c) and 5(d) for MNFG and MFNG alloys, respectively, at ambient pressure; Figs. 5(e) and 5(f) and Figs. 5(g) and 5(h) for MNFG and MFNG alloys, respectively, at $P = 6$ kbar. The restricted regions are plotted here for the better visibility of the magnetic satellite reflections. In addition to the first-order structural transition (from orthorhombic to hexagonal structure), several other interesting features have also been noticed, namely, (i) the position of all the magnetic satellite peaks remain almost unchanged with increasing T in ambient pressure; (ii) the application of 6 kbar of P results in an increase in the d values for $(101)^+$, $(-101)^-$, and $(000)^\pm$ peaks and decrease in the d values for $(101)^-$ and $(-101)^+$ peaks with increasing T; (iii) a notable amount of decrease (∼60 K decrease for MNFG and reduction of ∼ 50 K for MFNG) in magneto-structural transition temperature under external P has also been observed [see Fig. 6(a) phase fraction versus the T curve in the presence of 6 kbar of P]; and (iv) peak intensities of the magnetic reflections show monotonically decreasing behavior for the MNFG alloy in the martensitic phase; however, it is nonmonotonic for the MFNG alloy. The magnetic transition temperature of the orthorhombic phase falls within the same range as the structural transition temperature. Still, it cannot be reliably determined from the neutron diffraction data since the fraction of this phase rapidly decreases above MPT.

The T-dependent NPD data recorded for the MNFG alloy confirms the absence of any change in magnetic structure with sample temperature in ambient pressure as well as in the presence of external P. However, a clear change of the modulation of the AFM structure is found to be associated with the MFNG alloy with increasing T. The cycloidal modulation of the MFNG alloy remains unchanged up to 100 K. Further increase in the sample T results in a gradual rotation of the Mn moment from ab-plane to bc-plane and eventually the rotation was found to be completed at 190 K in ambient condition.

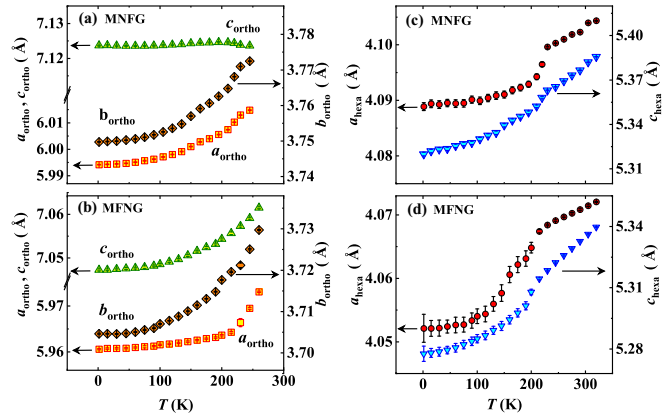

FIG. 6. (a), (b) show the variation of orthorhombic lattice parameters as a function of temperature (T) for MNFG and MFNG alloys, respectively. The T variation of hexagonal lattice parameters are plotted in (c), (d) for MNFG and MFNG alloys, respectively.

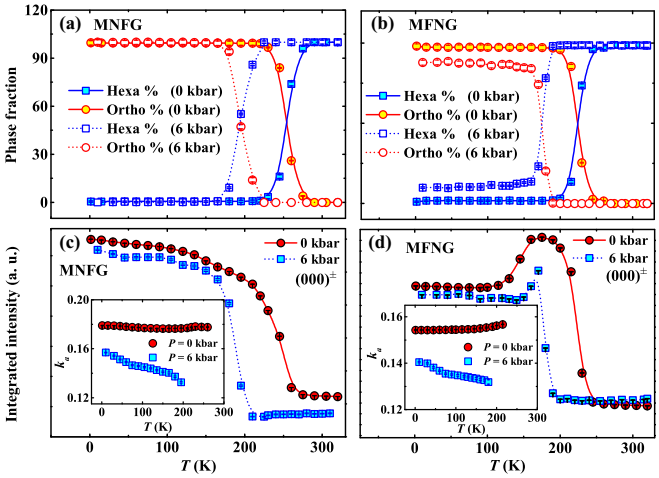

FIG. 7. Temperature variation of phase fraction both in ambient as well as in the presence of 6 kbar of external pressure (P) are depicted in (a), (b) for MNFG and MFNG alloys, respectively. The main panels of (c), (d) indicate integrated intensities of $(000)^{\pm}$ magnetic satellite reflection (both in ambient and high P situation) for MNFG and MFNG alloys, respectively. Insets of (c), (d) show the T variation of the x component of propagation vector k_a in ambient and high P situations for MNFG and MFNG alloys, respectively.

The application of external P has a remarkable effect on such rotation of the plane of the Mn moment. In the presence of 6 kbar of external P, the plane of the Mn-moment starts to rotate from 140 K and is eventually completed at 170 K. This behavior indicates that the external pressure prefers cycloidal modulation over helical modulation in MFNG. To probe such rotation, we used polar coordinates for magnetic structural analysis. Apart from the effect on the magnetic structure, we noticed a monotonic increase in the orthorhombic and hexagonal lattice parameters with T for both the alloys in an ambient and high-pressure situation. The T variation of lattice parameters in ambient conditions is shown in Fig. 6. Lattice parameters obtained in the presence of 6 kbar of external P are not plotted here for clear visualization. A change in slope is found to be associated with the hexagonal lattice parameters around the MPT. The variation of the lattice parameters observed for the present alloys is similar to that of the Ge-site doped MnNiGe alloys reported recently by our group [28].

Successful refinement of the NPD data also allowed us to estimate the T evolution of hexagonal (Ni_2In type), orthorhombic (TiNiSi type) and $MnNi_{1.3}Ge_{0.7}$ ($MgZn_2$-type hexagonal) phase fractions in the ambient and high-P situations. T variation of the phase fraction for MNFG and MFNG alloys are plotted in Figs. 7(a) and 7(b), respectively. A notable shift in the MPT temperature was observed for both the alloys in the presence of external P. The MPT temperatures observed here match well with the previously reported data [8]. Interestingly, not much change in the Mn-site moment size due to external P was noticed in the low-T martensitic phase in any of the alloys (see Table II). Notably, the application of P results in an increment in Ni_2In-type hexagonal phase fraction below the MPT region for the MFNG alloy and we observed about 9.83 wt% of Ni_2In-type hexagonal phase at 10 K in the presence of 6 kbar of external P. No such increase in high-T hexagonal austenite phase fraction below MPT in the case of MNFG alloy. The phase fraction for $MnNi_{1.3}Ge_{0.7}$ ($MgZn_2$-type hexagonal) phase remains almost unchanged with T. Such behavior matches well with the similar phase observed in Ge-site doped MnNiGe alloys [28]. We checked the existence of any magnetically ordered hexagonal phase both in ambient and high-P conditions. But we have not been able to detect any magnetic reflection corresponding to the hexagonal austenite phase in any of the alloys (both below and above MPT) though a significant hexagonal phase fraction is found to present (∼9.83 wt%) at 10 K in high-P condition for the MFNG alloy. Such an observation confirms that the present alloy transforms from an antiferromagnetically ordered orthorhombic phase to a paramagnetic hexagonal phase. This is unlike the Ge-Site doped MnNiGe alloys, where a commensurate AFM ordering had been observed for the high-T Ni_2In-type hexagonal austenite phase [28].

To shed more light on the T evolution of the magnetic structure, the integrated intensity of the $(000)^{\pm}$ magnetic reflection has been calculated for both the alloys and plotted as a function of T [see main panels of Figs. 7(c) and 7(d)]. The P induced shift in the structural transition temperature, which shows a one-to-one correspondence with the orthorhombic phase fraction, is further confirmed from such T-dependent integrated intensity data. Besides, we observed a sluggish decrease in the integrated intensities of the $(000)^{\pm}$ magnetic reflection with T up to MPT region for the MNFG alloy both in ambient and high-P conditions. The situation is slightly different for the MFNG alloy where, at ambient pressure, the integrated intensity remains almost unchanged till 100 K followed by a significant increase in it up to 190 K. Further increase of T results in a sharp decrease in it and eventually vanishes around 245 K. The overall nature of the integrated intensity versus T curve remains unchanged in the presence of external P. However, the intensity starts to increase above 150 K and shows the peak-like feature at 170 K. Eventually, the intensity for the $(000)^{\pm}$ vanishes at 200 K. We also noticed similar temperature variation of the integrated intensities for other magnetic satellite reflections (not shown here). The behavior of integrated intensity variation for MNFG alloy matches with other reported MEAs. In contrast, the nonmonotonic variation observed for the MFNG alloy is rare in the MEA family [28]. The rotation of Mn moments from the *ab* to *bc* plane may play the critical role behind the observed nonmonotonicity of the integrated intensities as the critical temperatures of Mn-moment rotation match well with the anomalies observed in the integrated intensity verus T plots, both in ambient and high-pressure conditions. A rotation of the axis of the helix from *a*-axis to *bc*-plane has been reported for some Mn-site doped MEAs [22–24].

Our refinement analyses also helped us to extract detailed information about the variation of the propagation vector as a function of T for both the alloys in the ambient and high-P situations. Not much variation in the propagation vector was observed in any of the alloys in ambient conditions with increasing sample T [see insets of Figs. 7(c) and 7(d)]. Such behavior is unlike the Si, Ti, Al, and Ga-doped MnNiGe alloys, where a significant increase in propagation vector was reported [21–23,28]. However, the 11% Cr-doped MnNiGe

alloy shows a striking similarity with the variation of the propagation vector with T [24]. Interestingly, the x component of the propagation vector k_a shows a significant decrease (monotonic) with T in the presence of 6 kbar of external P. For the MNFG alloy, k_a is found to change from 0.1569(1) at 10 K to 0.1325(8) at 200 K. On the other hand, for the MFNG alloy, the value of k_a at 10 K and 180 K are found to be 0.1404(8) and 0.1318(7), respectively. We also estimated the value of α at all temperatures in ambient as well as in high-P condition. The observed values of α are as follows: (i) for MNFG, $\alpha \sim 31.95^\circ$ at 260 K and 23.75° at 200 K for $P =$ 0 and 6 kbar, respectively, and (ii) for MFNG, $\alpha \sim 28.18^\circ$ at 215 K and 23.68° at 180 K for $P = 0$ and 6 kbar, respectively.

IV. DISCUSSIONS AND CONCLUSION

The ambient and high-P NPD measurements on Fe-doped MnNiGe alloys reveal several interesting features, namely, (i) incommensurate AFM ordering of the low-T martensite phase with helical and cycloidal modulation in MNFG and MFNG alloys, respectively, (ii) P induced increase in austenite phase fraction below the MPT region, (iii) almost unchanged propagation vector with T in ambient condition, (iv) monotonically decreasing propagation vector with T in the presence of external P, and (v) external P induced decrease in $\mathbf{k}$ and hence in α. The helically modulated AFM structure is not uncommon among MEAs, and such a structure has already been reported for pure and doped MEAs [21–24,28]. Notably, the axis of the helix remains along the a-axis in the entire martensitic phase for MNFG, which is similar to that of the Ge-site doped MnNiGe alloys [28]. However, some of the previous reports indicated a rotation of the axis of the helix form a-axis to bc-plane above a certain temperature, which was found to be absent for the Ni site Fe-doped alloy [22–24]. Our recent work on the Al and Ga-doped MnNiGe alloys also reveals the absence of such a rotation of the axis of the helix with increasing sample T [28]. On the other hand, the observation of cycloidal modulation in the MFNG alloy is the occasional one. Interestingly, a rotation in the plane of Mn-moments (from ab to bc plane) with increasing T was noticed for the MFNG alloy, which leads to the change in the modulation of the incommensurate AFM structure from cycloidal to helical. An increase in the hexagonal phase fraction at the low-T region in the presence of external P indicates that the application of P prefers the hexagonal phase over the low-T orthorhombic phase, which is also clear from the decrease in MPT in the high-P condition. External P is found to have a similar effect as that of the chemical pressure (doping), which is clear from the decrease in MPT for both cases [8].

The almost unchanged value of the x-component of propagation vector k_a with sample temperature is one of the crucial observations of the presently studied Fe-doped alloys. Such behavior indicates the unchanged strength of the magnetic interactions present in these alloys. This is unlike most of the MEAs reported earlier, where a significant increase in k_a was observed with T. Recent observations of helical magnetic structures in Ti and Cr-doped MEAs were analyzed based on the available theoretical models [23,24,37,38]. Competing exchange interactions often lead to such a type of helical magnetic structure. The moment direction rotates by a certain angle while going from one layer to another layer along the direction of the propagation vector. For the presently studied alloys, this rotation of the adjacent spins of Mn atoms depends strongly on T under high-P conditions, while a negligible change was observed in ambient conditions.

The theoretical framework proposes the axial next-nearest-neighbor Ising model that incorporates anisotropic competing exchange interactions in such a way that the spins are coupled by nearest-neighbor FM interaction in a plane perpendicular to the modulation axis of the helical/cycloidal magnetic structure. The spins are coupled by nearest-neighbor FM and next-nearest-neighbor AFM interactions along the modulation axis, leading to the helical/cycloidal phase. A stable helical/cycloidal structure is obtained for the condition $\cos\alpha = -\frac{J_1}{4J_2}$, where α is the angle between two adjacent spins of Mn atoms and J_1, J_2 signify the ferromagnetic and antiferromagnetic interactions, respectively, along the modulation axis [38]. A similar modulated helimagnetic phase was also observed in Tb, Dy, and Ho rare-earth elements, where alike competing interactions were also monitored [39]. In the present work, the values of α at different constant T are estimated for both the alloys in ambient as well as in high-P conditions. Penca *et al.* recently used the relation $\alpha = 180^\circ \cdot k_a$ for some doped MEAs [23,24]. A similar relation is found to be valid for the presently studied alloys also. From the stability criteria of the helical modulation, it is evident that any decrease in α is due to the increase in J_1/J_2 ratio. Using the values of α obtained from the NPD analysis, we calculated the values of the J_1/J_2 ratio both in ambient as well as in high-pressure conditions for the presently studied alloys at different constant T. The almost unchanged values of the J_1/J_2 ratio in ambient condition for both the alloys is consistent with the x component of the wave vector (at ambient P, for MNFG: $\frac{J_1}{J_2} \approx 3.38$ and 3.39 at 1.5 K and 260 K, respectively, and for MFNG: $\frac{J_1}{J_2} \approx 3.52$ and 3.53 at 1.5 K and 215 K, respectively). Such behavior signifies the unaltered AFM and FM strength with increasing sample temperature. Previous reports on Ge-site doped MnNiGe alloys indicate a steady decrease in J_1/J_2 ratio with increasing sample T implying the strengthening of AFM interaction with increasing sample T [28]. However, the scenario is entirely different in the presence of external P. At the low-T region, we observed an increase in the J_1/J_2 ratio with the application of external P. The value of the ratio further increases with increasing sample T for both MNFG and MFNG alloys (at $P = 6$ kbar, for MNFG: $\frac{J_1}{J_2} \approx 3.53$ and 3.66 at 10 K and 195 K, respectively, and for MFNG: $\frac{J_1}{J_2} \approx 3.58$ and 3.67 at 10 K and 180 K, respectively). The increase in the $\frac{J_1}{J_2}$ ratio signifies weakening of the AFM strength compared to the FM strength under external P. This is consistent with the decrease in α with increasing sample T under high-P conditions. This indicates that the alloys are going towards the parallel arrangement of magnetic spins (i.e., ferromagnetically ordered state) in the presence of external P.

In conclusion, the NPD analysis of two Fe-doped MnNiGe alloys of nominal compositions $MnNi_{0.75}Fe_{0.25}Ge$ and $Mn_{0.85}Fe_{0.15}NiGe$ in ambient as well as in the presence of 6 kbar of external P reveals a clear picture of the magnetic

structures at different phases. Both ambient and high-pressure data confirm that the low-T orthorhombic phase shows incommensurate antiferromagnetic ordering with helical and cycloidal modulation for the MNFG and MFNG alloys, respectively. The axis of the modulation is found to be along the a-axis throughout the magnetically ordered region for both the alloys. On the other hand, no signature of the magnetically ordered hexagonal phase was observed in any of the alloys down to 1.5 K, the lowest achievable T during the measurement. The magnetic spin arrangement of the Mn atoms remains unchanged even in the presence of external P without the presence of any new set of magnetic reflections in the NPD pattern for both the alloys. However, the application of P results in a significant decrease in the propagation vectors. Such a reduction in the propagation vectors plays a crucial role in reducing the angle between the two adjacent Mn spins of the helix/cycloid and, hence, decreasing the next-nearest-neighbor AFM interaction along the direction of the propagation vector. This indicates that external P prefers a parallel spin arrangement, and with sufficiently high P, ferromagnetic ordering can be achieved for both MNFG and MFNG alloys.

Neutron diffraction data were recorded on the WISH diffractometer at the ISIS Neutron and Muon Source. Information on the data can be accessed through the STFC ISIS Facility [40,41].

ACKNOWLEDGMENTS

SC and RR would like to thank the Science and Engineering Research Board (SERB), DST-India, for financial support (Project No. CRG/2020/000670). SC, SCD, and KM would like to thank UK Newton funding and DST-India (SR/NM/Z-07/2015) for the access to the experimental facility and financial support to carry out the experiments, and Jawaharlal Nehru Centre for Advanced Scientific Research (JNCASR) for managing the DST-India project. KM (IF160051) and SCD (IF160587) would like to thank DST-India for their inspire fellowship. JS would like to thank the European Unions Horizon 2020 research and innovation program under the Marie Skłodowska-Curie Grant Agreement (GA) No. 665593 awarded to the Science and Technology Facilities Council. JS would also like to thank SERB, DST-India for a Ramanujan Fellowship [RJF/2019/000046(SQUID-1986-JS-3632)].

[1] C. L. Zhang, D. H. Wang, Q. Q. Cao, Z. D. Han, H. C. Xuan, and Y. W. Du, Appl. Phys. Lett. **93**, 122505 (2008).
[2] K. Koyama, M. Sakai, T. Kanomata, and K. Watanabe, Jpn. J. Appl. Phys. **43**, 8036 (2004).
[3] C. Zhang, D. Wang, Q. Cao, S. Ma, H. Xuan, and Y. Du, J. Phys. D: Appl. Phys. **43**, 205003 (2010).
[4] P. Dutta, S. Pramanick, D. Venkateshwarlu, V. Ganesan, S. Majumdar, D. Das, and S. Chatterjee, Europhys. Lett. **108**, 17012 (2014).
[5] T. Samanta, I. Dubenko, A. Quetz, S. Temple, S. Stadler, and N. Ali, Appl. Phys. Lett. **100**, 052404 (2012).
[6] N. T. Trung, L. Zhang, L. Caron, K. H. J. Buschow, and E. Brück, Appl. Phys. Lett. **96**, 172504 (2010).
[7] P. Dutta, S. Pramanick, S. Majumdar, D. Das, and S. Chatterjee, J. Magn. Magn. Mater. **395**, 312 (2015).
[8] E. Liu, W. Wang, L. Feng, W. Zhu, G. Li, J. Chen, H. Zhang, G. Wu, C. Jiang, H. Xu, and F. de Boer, Nat. Commun. **3**, 873 (2012).
[9] L. Caron, N. T. Trung, and E. Brück, Phys. Rev. B **84**, 020414(R) (2011).
[10] I. Dincer, E. Yüzüak, G. Durak, Y. Elerman, A. M. T. Bell, and H. Ehrenberg, J. Alloys Compd. **540**, 236 (2012).
[11] N. T. Trung, V. Biharie, L. Zhang, L. Caron, K. H. J. Buschow, and E. Brück, Appl. Phys. Lett. **96**, 162507 (2010).
[12] J. Wang, D. Wang, C. Chen, O. Nashima, T. Kanomata, H. Mizuseki, and Y. Kawazoe, Appl. Phys. Lett. **89**, 262504 (2006).
[13] P. Dutta, S. Pramanick, V. Singh, D. T. Major, D. Das, and S. Chatterjee, Phys. Rev. B **93**, 134408 (2016).
[14] P. Dutta, S. Pramanick, D. Das, and S. Chatterjee, J. Phys. D: Appl. Phys. **49**, 385001 (2016).
[15] K. Mandal, P. Dutta, P. Dasgupta, S. Pramanick, and S. Chatterjee, J. Phys. D: Appl. Phys. **51**, 225004 (2018).
[16] K. Mandal, S. C. Das, P. Dutta, S. Pramanick, P. Dasgupta, and S. Chatterjee, J. Appl. Phys. **124**, 215904 (2018).
[17] K. Mandal, S. C. Das, P. Dutta, S. Pramanick, and S. Chatterjee, J. Alloys Compd. **822**, 153454 (2020).
[18] S. C. Das, K. Mandal, P. Dutta, S. Pramanick, and S. Chatterjee, J. Phys. D: Appl. Phys. **51**, 065002 (2018).
[19] S. C. Das, K. Mandal, P. Dutta, S. Pramanick, and S. Chatterjee, J. Magn. Magn. Mater. **465**, 44 (2018).
[20] W. Bażela, A. Szytuła, J. Todorović, Z. Tomkowicz, and A. Zięba, Phys. Status Solidi A **38**, 721 (1976).
[21] W. Bażela, A. Szytuła, J. Todorović, and A. Zięba, Phys. Status Solidi A **64**, 367 (1981).
[22] W. Bażela and A. Szytuła, Phys. Status Solidi A **66**, 45 (1981).
[23] B. Penc, A. Hoser, S. Baran, R. Duraj, M. Marzec, T. J. Gołąb, A. Szytuła, V. Dyakonov, N. Nedelko, A. Sivachenko, K. Dyakonov, W. Bażela, and H. Szymczak, Phase Transitions **91**, 1107 (2018).
[24] B. Penc, A. Hoser, S. Baran, and A. Szytuła, Phase Transitions **91**, 118 (2018).
[25] A. Quetz, T. Samanta, I. Dubenko, M. J. Kangas, J. Y. Chan, S. Stadler, and N. Ali, J. Appl. Phys. **114**, 153909 (2013).
[26] C. L. Zhang, Z. D. Han, B. Qian, H. F. Shi, C. Zhu, J. Chen, and T. Z. Wang, J. Appl. Phys. **114**, 153907 (2013).
[27] E. Liu, Y. Du, J. Chen, W. Wang, H. Zhang, and G. Wu, IEEE Trans. Magn. **47**, 4041 (2011).
[28] S. C. Das, J. Sannigrahi, P. Dutta, S. Pramanick, D. Khalyavin, D. T. Adroja, and S. Chatterjee, Phys. Rev. B **103**, 094422 (2021).
[29] A. Szytuła, A. T. Pędziwiatr, Z. Tomkowicz, and W. Bażela, J. Magn. Magn. Mater. **25**, 176 (1981).
[30] L. C. Chapon, P. Manuel, P. G. Radaelli, C. Benson, L. Perrott, S. Ansell, N. J. Rhodes, D. Raspino, D. Duxbury, E. Spill, and J. Norris, Neutron News **22**, 22 (2011).
[31] V. F. Sears, Neutron News **3**, 26 (1992).
[32] J. Rodríguez-Carvajal, Physica B: Condens. Matter **192**, 55 (1993).

[33] Y. V. Kuźma, M. Y. Teslyuk, and E. I. Gladyshevskii, J. Struct. Chem. **3**, 143 (1962).
[34] E. F. Bertaut, Acta Cryst. A **24**, 217 (1968).
[35] Y. A. Izyumov, V. E. Naish, and R. P. Ozerov, *Neutron Diffraction of Magnetic Materials* (Plenum, New York, 1991).
[36] Y. A. Izyumov and V. E. Naish, J. Magn. Magn. Mater. **12**, 239 (1979).
[37] A. Herpin, P. Meriel, and J. Villain, J. Phys. Radium. **21**, 67 (1960).
[38] U. Enz, J. Appl. Phys. **32**, S22 (1961).
[39] T. Chattopadhyay, Science **264**, 226 (1994).
[40] S. Chatterjee, D. T. Adroja, S. C. Das, K. Mandal, D. Khalyavin, J. Sannigrahi, and S. Pramanick, STFC ISIS Neutron and Muon Source, 10.5286/ISIS.E.RB1820028 (2018).
[41] S. Chatterjee, J. Sannigrahi, S. Pramanick, N. Khamaru, S. C. Das, D. T. Adroja, D. Khalyavin, and P. Dutta, STFC ISIS Neutron and Muon Source, 10.5286/ISIS.E.RB1968022 (2019).